THE GEOLOGICAL SOCIETY OF AMERICA®

Astronomical and tectonic influences on climate and deposition revealed through radioisotopic geochronology and Bayesian age-depth modeling of the early Eocene Green River Formation, Wyoming, USA

Benjamin T. Bruck[1], Brad S. Singer[1†], Mark D. Schmitz[2], Alan R. Carroll[1], Stephen Meyers[1], Andrew P. Walters[1,3], and Brian R. Jicha[1]

[1]*Department of Geoscience, University of Wisconsin–Madison, 1215 West Dayton Street, Madison, Wisconsin 53706, USA*
[2]*Department of Geosciences, Boise State University, 1910 University Drive, Boise, Idaho 83725, USA*
[3]*Department of Geosciences, University of Arizona, 1040 East 4th Street, Tucson, Arizona 85721, USA*

ABSTRACT

The Wilkins Peak Member (WPM) of the Green River Formation in Wyoming, USA, comprises alternating lacustrine and alluvial strata that preserve a record of terrestrial climate during the early Eocene climatic optimum. We use a Bayesian framework to develop age-depth models for three sites, based on new $^{40}Ar/^{39}Ar$ sanidine and $^{206}Pb/^{238}U$ zircon ages from seven tuffs. The new models provide two- to ten-fold increases in temporal resolution compared to previous radioisotopic age models, confirming eccentricity-scale pacing of WPM facies, and permitting their direct comparison to astronomical solutions. Starting at ca. 51 Ma, the median ages for basin-wide flooding surfaces atop six successive alluvial marker beds coincide with short eccentricity maxima in the astronomical solutions. These eccentricity maxima have been associated with hyperthermal events recorded in marine strata during the early Eocene. WPM strata older than ca. 51 Ma do not exhibit a clear relationship to the eccentricity solutions, but accumulated 31%–35% more rapidly, suggesting that the influence of astronomical forcing on sedimentation was modulated by basin tectonics. Additional high-precision radioisotopic ages are needed to reduce the uncertainty of the Bayesian model, but this approach shows promise for unambiguous evaluation of the phase relationship between alluvial marker beds and theoretical eccentricity solutions.

Brad S. Singer https://orcid.org/0000-0003-3595-5168
†bsinger@wisc.edu

INTRODUCTION

Deep-time geologic records of warming climate provide analogs for how Earth systems will respond to rising temperature in the future. The highest temperatures and atmospheric CO_2 levels of the Cenozoic occurred during the early Eocene, including the early Eocene climatic optimum (EECO) (ca. 53–49 Ma; Zachos et al., 2008; Lauretano et al., 2018; Zhu et al., 2019). Superimposed over the long-term warming trends of the EECO are hyperthermal events, transient periods of global warming which are associated with large-scale releases of CO_2 to the ocean and atmosphere and the negative excursions in the carbon isotope record that accompany them (Zeebe et al., 2009; McInerney and Wing, 2011). In the marine record, hyperthermal events have been associated with eccentricity maxima, with the suggestion that eccentricity-modulated seasonality drives increased precipitation, weathering, and sedimentary discharge to the shallow marine environment (Cramer et al., 2003; Zachos et al., 2010; Lauretano et al., 2016, 2018). The dissolution of carbonate material associated with ocean acidification has left offshore strata more condensed than terrestrial or near-shore records, frustrating attempts to identify astrochronological signals in deep marine records (e.g., Westerhold et al., 2017). In contrast, the Wilkins Peak Member (WPM) of the Green River Formation (GRF), Wyoming, USA, records deposition in an alkaline lake (sustained pH >10; Jagniecki et al., 2015), and thus provides a record that is relatively uncompromised by rising atmospheric CO_2, and so is greatly expanded compared to equivalent deep marine sections. Excellent surface exposure of the WPM, numerous drill cores, and a laterally continuous system of distinct bedding surfaces across the basin which permit clear correlation from outcrop to core, provide a high-resolution record of the changing Eocene climate (Culbertson, 1961; Pietras and Carroll, 2006) (Fig. 1). Additionally, the WPM records a portion of the EECO which coincides with the estimated age of a resonance transition in orbital solutions (Laskar et al., 2011; Zeebe and Lourens, 2019). Identifying and radioisotopically constraining the ages of astronomically influenced sedimentary features may provide insights into the validity and accuracy of these astronomical solutions and offer methods to test future solutions.

The WPM is characterized by lithological cycles which have long been interpreted to reflect astronomically forced lake expansion and contraction (e.g., Bradley, 1929; Fischer and Roberts, 1991; Meyers, 2008; Machlus et al., 2008; Aswasereelert et al., 2013). Lake deposits alternate with nine distinctive alluvial intervals that are topped with flooding surfaces, and so were likely deposited during major lowstands (termed marker beds A–I; Culbertson, 1961; Pietras and Carroll, 2006). Prior work has found strong associations between these marker beds and eccentricity (Smith et al., 2010; Aswasereelert et al., 2013). Negative $\delta^{13}C$ excursions in similar Uinta basin (Wyoming, USA) deposits suggest that the alluvial intervals record deposition during hyperthermals (Smith et al., 2014; Birgenheier et al., 2020). Using the first $^{206}Pb/^{238}U$ zircon ages for WPM tuffs, and comparisons of a radioisotopic age model to the astronomical solutions of Laskar et al. (2004) and Smith et al. (2010, 2014) proposed that alluvial sedimentation occurred during minima in short eccentricity. In contrast, Eocene hyperthermals expressed in marine deposits have been interpreted to correspond

GSA Bulletin;
published online 16 March 2023

https://doi.org/10.1130/B36584.1; 11 figures; 1 table; 1 supplemental file.

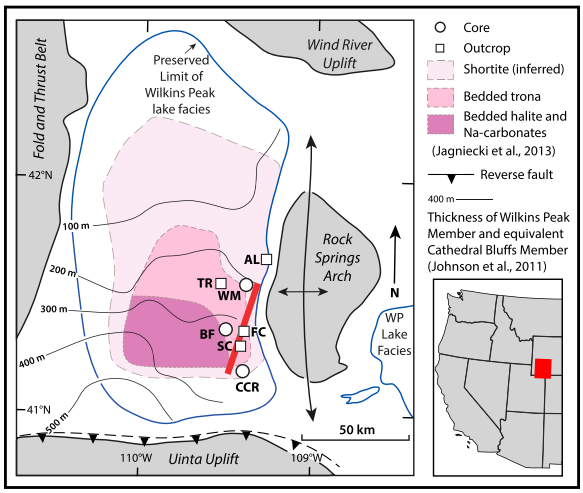

Figure 1. Location of cores (circles) and extent of the Wilkins Peak (WP) Member in the Bridger Basin, Wyoming, USA. Abbreviations of core names: BF, Energy Research and Development Administration-Laramie Energy Research Center Blacks Fork 1; CCR, U.S. Department of Energy-Laramie Energy Technology Center Currant Creek Ridge-1; WM, White Mountain (designated BF-1, CCR-1, and WM in the text). Outcrop sampling locations: TR, Tollgate Rock (Main, Layered, and Sixth tuffs); AL, Apache Lane (Grey tuff); FC, Firehole Canyon (Firehole tuff); SC, Sage Creek (Second tuff). The transect from Figure 2 is denoted by a thick red line.

with short eccentricity maxima (Cramer et al., 2003; Zachos et al., 2010; Piedrahita et al., 2022). To resolve this question and to capitalize on the record of climate change preserved in the WPM, a highly resolved timescale of lacustrine deposition is required.

GEOLOGICAL AND GEOCHRONOLOGICAL CONTEXT

The GRF occupies intramontane basins located in modern-day Wyoming, Colorado, and Utah (USA). In the Bridger Basin of southwestern Wyoming this formation was deposited by the ancient Lake Gosiute, and is subdivided into four members: the Luman, Tipton, Wilkins Peak, and Laney. The first and last of these represent overfilled lake conditions, and generally consist of deposits associated with lacustrine high stand and fresh water (Pietras and Carroll, 2006). The middle member, the Wilkins Peak, represents deposition by an underfilled lake, and its deposits are characterized by cyclic emplacement of oil shale, evaporite (i.e., trona and halite), mudstone, and siliciclastic marker beds, which have been interpreted as recurring periods of evaporation and lake expansion (Culbertson, 1961; Fischer and Roberts, 1991; Roehler, 1992; Pietras and Carroll, 2006) (Figs. 1–3). WPM lacustrine strata are intercalated with numerous volcanic tuffs, permitting precise radioisotopic dating (Smith et al., 2008, 2010, 2014; Machlus et al., 2004, 2015). Radioisotopic dating efforts in the WPM have largely focused on seven major tuffs: the Firehole, Second, Boar, Grey, Layered, Main, and Sixth tuffs (Smith et al., 2008; Machlus et al., 2008, 2015). The enclosing system of laterally continuous alluvial marker beds, throughout the basin (e.g., Culbertson, 1961) and the extent to which these tuffs have been characterized and described by prior work, permit the identification of these tuffs in both outcrop and drill cores. This stratigraphic framework allows for detailed inter-site correlation with great confidence across the Bridger Basin (Smith et al., 2008, 2010, 2014, 2015) (Fig. 2). However, efforts to develop a high-resolution chronology for the basin have been hampered by both insufficient precision, and by systematic intercalibration uncertainties between radioisotopic clocks. U-Pb dating by Machlus et al. (2015) approached the precision necessary to link astronomical cycles with lithologic cyclicity, but found significant discrepancies between U-Pb and previous $^{40}Ar/^{39}Ar$ age models. Notably, the Machlus et al. (2015) $^{206}Pb/^{238}U$ ages for the Sixth, Layered, and Main tuffs are younger than the corresponding Smith et al. (2010) $^{40}Ar/^{39}Ar$ ages. Machlus et. al. (2015) interpreted the Smith et al. (2010) multicrystal dates to have been biased by recycling and inheritance of older crystals (e.g., Wotzlaw et al., 2013; Rivera et al., 2014).

We present a new suite of $^{206}Pb/^{238}U$ and $^{40}Ar/^{39}Ar$ dates from seven tuffs in the WPM that are correlated into three drill cores spanning the basin (Roehler, 1992). Our new geochronologic data and age models improve upon prior work in two key ways: (1) an increase in precision and accuracy due to improvements in the chemical abrasion–isotope dilution–thermal ionization mass spectrometry (CA-ID-TIMS) methodology in the case of U-Pb zircon dating, and improved mass spectrometry in the case of $^{40}Ar/^{39}Ar$ dating, and (2) the integration of both chronometers using a Bayesian approach that employs the principle of superposition to further constrain a posterior probabilistic age-depth model (Trayler et al., 2020; Haslett and Parnell, 2008). We leverage these advances to quantitatively evaluate the relationship between eccentricity forcing and sedimentation in the WPM, with implications for terrestrial climate response during Eocene hyperthermal events.

METHODS

Tuffs were collected from four localities: Sage Creek, Firehole Canyon, Apache Lane, and Tollgate Rock (Fig. 1). At Boise State University (Idaho, USA), zircon grains from seven samples were imaged using cathodoluminescence (CL) and subsequently pre-screened by in situ laser ablation–inductively coupled plasma–mass spectrometry (LA-ICP-MS) dating. Since many of the crystals selected for analysis were small, 2 by 12 by 60 μm trenches transecting the crystal rims and cores were ablated, rather than spots. Zircon crystals that did not yield anomalously old LA-ICP-MS ages, and appeared to be free

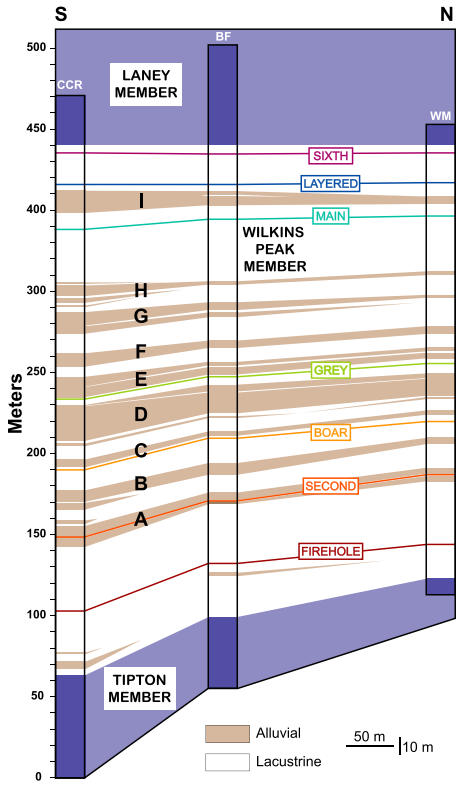

Figure 2. Simplified stratigraphy for the Wilkins Peak Member of the Green River Formation (Wyoming, USA) adapted from Smith et al. (2015), showing the correlation of alluvial beds and tuffs between the Currant Creek Ridge (CCR), Blacks Fork (BF), and White Mountain (WM) cores.

Figure 3. Outcrop photo from the air looking north showing the succession of alluvial "marker beds" D through I in the Wilkins Peak Member (Wyoming, USA). Forest service road 106 traverses the base of this section.

of older inherited components in CL imaging, were then dated by CA-ID-TIMS. Complete CL imagery and LA-ICP-MS data for each tuff, as well as a summary of LA-ICP-MS screening results (Table S1[1]) and full CA-ID-TIMS analytical data (Table S2), may be found in the Supplemental Material. Sanidine crystals from two samples were irradiated for 80 h along with the 28.201 ± 0.046 Ma Fish Canyon sanidine (Kuiper et al., 2008), and dated at the University of Wisconsin–Madison (Wisconsin, USA) WiscAr Laboratory using a Noblesse multi-collector mass spectrometer (Jicha et al., 2016; Supplemental Material, see footnote 1). The ^{40}K total decay constant of 5.463 ± 0.107 × 10^{-10}/yr of Min et al. (2000) was used to calculate ages. Several dozen crystals of Fish Canyon sandine that were either co-located with the Grey and Main tuff crystals or from adjacent wells in a 2.38 cm diameter aluminum disk were measured to determine a mean J value for these samples (Table S3, Supplemental Material). Single crystal fusion experiments were performed on each sample to identify and exclude dates from older inherited or reworked crystals from the weighted mean age determinations.

Bayesian age-depth models of the WPM were developed for three separate drill cores using the modified BChron R package of Trayler et al. (2020). The position of tuffs and marker beds in each model represent their height above the base of the WPM (Aswasereelert et al., 2013; Smith et al., 2015). The stratigraphic positions of tuffs in each core are well-constrained due to an enclosing system of laterally continuous alluvial marker beds throughout the basin (e.g., Culbertson, 1961). Crucially, this Bayesian approach does not rely on astronomically tuning the sedimentary record—making assumptions about the sedimentation rate to fit astrochronological targets—and thus permits a more objective test for the association between sedimentary events and astronomical solutions for eccentricity. Moreover, the compound Poisson-gamma accumulation prior used for stochastic interpolation between dated horizons in this approach has been shown to effectively mimic both rapid deposition and near unconformity like events (Haslett and Parnell, 2008). Therefore, the 95% credible interval of the Bayesian model includes and constrains possible hiatuses and periods of highly variable rates of deposition.

Age models were produced for three cores through the WPM (Brownfield et al., 2011): the Blacks Fork 1 core (BF-1, U.S. Geological Survey (USGS) W0080, 41.35647°N, 109.52564°W); White Mountain 1 core (WM, USGS W0081, 41.550856°N, 109.418522°W); and Currant Creek Ridge 1 core (CCR-1, USGS W0420R, 41.181353°N, 109.606624°W). Each model uses the summed probability distribution of all analyses included in the weighted mean for each tuff as inputs for the dated horizons (Tables S2 and S3). ^{206}Pb/^{238}U and ^{40}Ar/^{39}Ar analyses for the Main and Grey tuffs were included as separate probability distributions in each model, as each chronometer represents an independent constraint on the age model at that given depth. All dated horizons were assigned a depth uncertainty of 0.1 m. Age-depth positions were predicted every 0.1 m. Ten-thousand age-depth paths were generated using Markov Chain Monte Carlo methods to produce a median age-depth model, and an associated 95% highest density interval (HDI) or credible interval, the Bayesian analogue to 2σ uncertainty (Trayler et al., 2020).

RESULTS AND DISCUSSION

Geochronology Results

From five to 13 single-zircon U-Pb CA-ID-TIMS dates were obtained from each tuff. From zircons that yield concordant ^{206}Pb/^{238}U and ^{207}Pb/^{235}U dates (Fig. 4), we focus on the ^{206}Pb/^{238}U dates because they are more precise and accurate (e.g., Mattinson, 2005). Firehole tuff sample 2017-59-FC shows no age dispersion, whereas other samples reveal only minor

[1]Supplemental Material. Figures S1–S14: Cathodoluminescence images of zircons from each of the seven tuffs highlighting crystals chosen for U-Pb dating experiments. Table S1: LA-ICP-MS screening of zircon. Table S2: Complete U-Th-Pb isotopic data from CA-ID-TIMS. Table S3: Complete ^{40}Ar/^{39}Ar isotopic data with probability density plots. Table S4: Comparison of U-Pb dating uncertainties. Table S5: Posterior ages for marker bed tops. Supplemental Data 1: Metadata for LA-ICPMS U-Pb analyses of zircon in Boar tuff sample 2017-62-FC. Supplemental Data 2: Metadata for LA-ICPMS U-Pb analyses of zircon in Grey tuff sample 2017-17-AL. Supplemental Data 3: Metadata for LA-ICPMS U-Pb analyses of zircon in Firehole tuff sample 2017-59-SC. Supplemental Data 4: Metadata for LA-ICPMS U-Pb analyses of zircon in Layered tuff sample TR-6. Supplemental Data 5: Metadata for LA-ICPMS U-Pb analyses of zircon in Main tuff sample 2016-8.1 TR. Supplemental Data 6: Metadata for LA-ICPMS U-Pb analyses of zircon in Second tuff sample 2017-60-SC. Supplemental Data 7: Metadata for LA-ICPMS U-Pb analyses of zircon in Sixth tuff sample 2016-14-TR. Please visit https://doi.org/10.1130/GSAB.S.21971060 to access the supplemental material, and contact editing@geosociety.org with any questions.

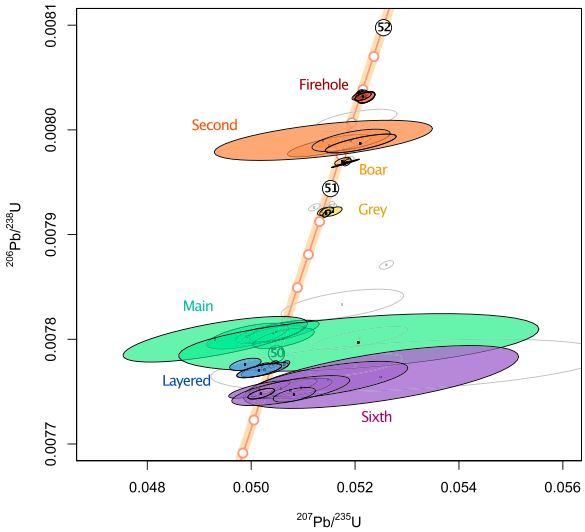

Figure 4. U-Pb concordia plots for dated tuffs in the Wilkins Peak Member of the Green River Formation, Wyoming, USA. Filled circles represent analyses included in weighted means. The orange band gives the 2σ uncertainty on the concordia curve.

age dispersion (Table 1). For each, the youngest group of concordant $^{206}Pb/^{238}U$ dates that passed the modified Thomson Tau outlier rejection criterion ($p = 0.05$) were selected for inclusion in a weighted mean that represents the closest approach to the eruption and deposition age of the tuff bed. Crystals returning older dates are excluded as inherited from earlier Paleogene volcanic rocks during magma genesis and/or eruption. Uncertainties for calculated weighted means are reported in the form ± X(Y)[Z] where X is the analytical contribution, Y is the combined analytical and tracer (EARTHTIME 2535; Condon et al., 2015; McLean et al., 2015) uncertainty, and Z combines analytical, tracer, and decay constant uncertainties (Table 1; Fig. 5; Table S2).

Single sanidine $^{40}Ar/^{39}Ar$ dates were obtained from the Main and Grey tuffs (Table 1, Fig. 5), with only one distinct outlier in each set of dates. The large uncertainties in the sanidine dates compared to the U-Pb dates from the same ash beds are due, in part, to the small size of the individual sanidine crystals fused (~75–100 μm). Single-crystal fusions are preferred in this case due to the prior concerns over inheritance and reworking in the multi-crystal analyses of Smith et al. (2008). Uncertainties for calculated weighted means are reported in the form ± X(Y)[Z] where X is the analytical contribution, Y is the combined analytical and J-value uncertainty, and Z combines analytical, J-value, and decay constant uncertainties (2σ; Jicha et al., 2016).

Firehole Tuff

Of 96 zircon crystals analyzed by LA-ICP-MS, one (1%) returned a Cretaceous $^{206}Pb/^{238}U$ age and was excluded from subsequent analyses. Eight grains were selected for CA-ID-TIMS analysis. All eight are concordant and have indistinguishable isotope ratios with a weighted mean $^{206}Pb/^{238}U$ age of 51.576 ± 0.007 (0.017) [0.058] Ma (mean square weighted deviate [MSWD] = 0.71; n = 8), that we interpret to reflect the time since the eruption and deposition of this tuff.

Second Tuff

Of 73 zircon crystals analyzed by LA-ICP-MS, 14 (19%) returned a Cretaceous $^{206}Pb/^{238}U$ age and were excluded from subsequent analyses. Five grains were selected for CA-ID-TIMS analysis. The four youngest are concordant and have indistinguishable isotope ratios with a weighted mean $^{206}Pb/^{238}U$ age of 51.286 ± 0.029 (0.039) [0.067] Ma (MSWD = 0.23; n = 4), which is interpreted to reflect the time since the eruption and deposition of this tuff.

Boar Tuff

Of 123 zircon crystals analyzed by LA-ICP-MS, 74 (60%) returned Cretaceous $^{206}Pb/^{238}U$ ages and were excluded from subsequent analyses. Eight grains were selected for CA-ID-TIMS analysis. The four youngest zircon dates are concordant and have indistinguishable isotope ratios with a weighted mean $^{206}Pb/^{238}U$ age of 51.171 ± 0.009 (0.018) [0.058] Ma (MSWD = 0.65; n = 4) that we interpret to reflect time since the eruption and deposition of this tuff.

Grey Tuff

Of 190 zircon crystals analyzed by LA-ICP-MS, 79 (42%) returned Cretaceous or older $^{206}Pb/^{238}U$ ages and were excluded from subsequent analyses. Initial pilot analysis of eight zircon crystals from the Grey tuff found a bimodal distribution of ages, with a younger population at ca. 50.86 Ma and an older population at ca. 50.90 Ma. An additional six zircons were selected for CA-ID-TIMS analysis, focusing on acicular euhedral crystals with dark outer rims, like those which produced the younger age population in the pilot analyses. Of the 10 crystals analyzed, the five youngest zircons are concordant and have indistinguishable isotope ratios with a weighted mean $^{206}Pb/^{238}U$ age of 50.864 ± 0.008 (0.027) [0.061] Ma (MSWD = 0.19; n = 5). We interpret the latter to be the best U-Pb age for eruption and deposition of this tuff.

Single-crystal laser-fusion experiments were performed on 30 sanidine crystals. The young-

TABLE 1. SUMMARY OF RADIOISOTOPIC AGES

Sample	Tuff	Latitude (°S)	Longitude (°W)	Altitude (masl)	N	MSWD	Wtd. mean age (Ma)	$\pm 2\sigma_{int}$	$\pm 2\sigma_{tr}$	$\pm 2\sigma_{tot}$
$^{206}U/^{238}Pb$ Results										
2016-14-TR	Sixth	41.54306	109.482389	1929	8/13	1.12	49.769	0.016	0.030	0.061
TR-6	Layered	41.54267	109.482111	1893	6/8	1.28	49.925	0.009	0.027	0.060
2016-8.1-TR	Main	41.54231	109.482194	1893	7/8	0.31	50.114	0.022	0.034	0.063
2017-17-AL	Grey	41.65648	109.289478	2154	5/10	0.19	50.864	0.008	0.027	0.061
2017-62-FC	Boar	41.35397	109.397986	1960	4/8	0.65	51.171	0.009	0.018	0.058
2017-60-SC	Second	41.29363	109.385742	1949	4/5	0.23	51.286	0.029	0.039	0.067
2017-59-FC	Firehole	41.35085	109.383578	1945	8/8	0.71	51.576	0.007	0.017	0.058
$^{40}Ar/^{39}Ar$ Results*								$\pm 2\sigma_{int}$	$\pm 2\sigma_{int+J}$	$\pm 2\sigma_{tot}$
2016-8.1-TR	Main	41.54231	109.482194	1893	33/34	0.87	50.133	0.038	0.048	0.078
2017-17-AL	Grey	41.65648	109.289478	2154	29/30	1.10	50.912	0.041	0.052	0.082

Notes: $\pm 2\sigma_{int}$—analytical uncertainty only at the 95% confidence interval; $\pm 2\sigma_{tr}$—analytical plus tracer uncertainty; $\pm 2\sigma_{tot}$—fully propagated uncertainty at the 95% confidence interval including analytical, tracer/standard age, and decay constant uncertainties; $\pm 2\sigma_{int+J}$—analytical uncertainty at the 95% confidence interval including J uncertainty; MSWD—mean square of weighted deviates; masl—meters above sea level.

*Ages were calculated relative to Fish Canyon sanidine interlaboratory standard at 28.201 Ma (Kuiper et al., 2008). The total ^{40}K decay constant and uncertainty of $5.463 \pm 0.107 \times 10^{-10}$/yr is from Min et al. (2000).

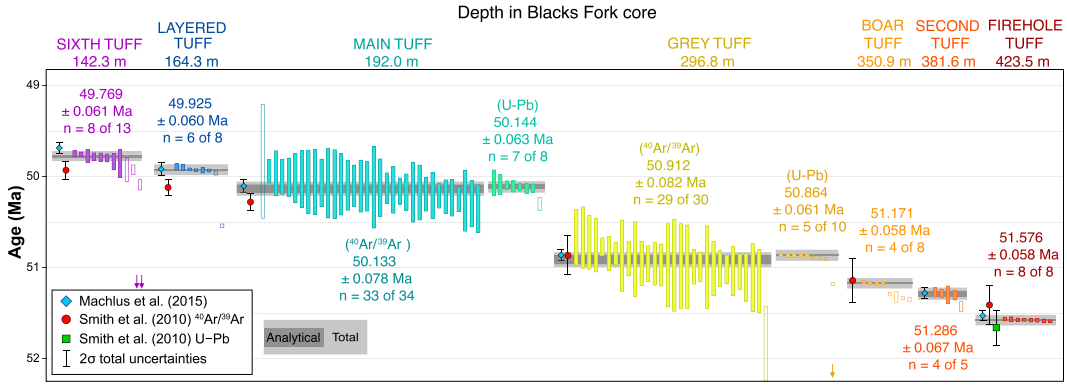

Figure 5. Comparison between U-Pb and $^{40}Ar/^{39}Ar$ geochronology of tuffs in the Wilkins Peak Member of the Green River Formation, Wyoming, USA. Solid bars represent 95% confidence interval single-crystal zircon chemical abrasion–isotope dilution–thermal ionization mass spectrometry dates (see Table S1) or single crystal sanidine fusions (see Table S2) presented in this study. Points represent multi-crystal and single-crystal weighted mean ages of Smith et al. (2010), and single-crystal weighted mean ages of Machlus et al. (2015). $^{40}Ar/^{39}Ar$ ages are re-calibrated from Smith et al. (2008) using an age of 28.201 Ma (Kuiper et al., 2008) for the Fish Canyon sanidine standard (Smith et al., 2010). All ashes were sampled at outcrop and correlated to the Blacks Fork core at noted depths (Smith et al., 2010). The arrows below data from the Sixth and Grey tuffs denote inherited zircons too old to show at this scale.

est population of 29 crystals yields a weighted mean age of 50.912 ± 0.041 (0.052) [0.078] Ma, with an MSWD of 0.87. We interpret this as a best $^{40}Ar/^{39}Ar$ estimate of the age of eruption and deposition of this tuff. For the Grey tuff and Main tuff (discussed next) the $^{206}Pb/^{238}U$ and $^{40}Ar/^{39}Ar$ ages are concordant with one another using the Y uncertainties, reflecting in part the large uncertainty in the ^{40}K total decay constant of Min et al. (2000). We note that were we to use the more precise ^{40}K total decay constant proposed by Renne et al. (2011), the $^{206}Pb/^{238}U$ and $^{40}Ar/^{39}Ar$ ages would be discordant for these two tuffs.

Main Tuff

Of 69 zircon crystals analyzed by LA-ICP-MS, 19 returned Cretaceous or older $^{206}Pb/^{238}U$ ages and were excluded from subsequent analyses. Eight zircon crystals were selected for CA-ID-TIMS analysis. The seven youngest zircon dates are concordant and have indistinguishable isotope ratios with a weighted mean $^{206}Pb/^{238}U$ age of 50.114 ± 0.022 (0.034) [0.063] Ma (MSWD = 0.31; n = 7), which is interpreted as the best U-Pb age for eruption and deposition of this tuff.

Single-crystal laser-fusion experiments were performed on 34 sanidine crystals. The youngest population of 33 crystals yield a weighted mean age of 50.133 ± 0.038 (0.048) [0.078] Ma, with an MSWD of 1.10. We interpret this as a best $^{40}Ar/^{39}Ar$ estimate of the age of eruption and deposition of this tuff.

Layered Tuff

Of 23 zircon crystals analyzed by LA-ICP-MS, eight (35%) returned Cretaceous or older $^{206}Pb/^{238}U$ ages and were excluded from subsequent analyses. Eight zircon crystals were selected for CA-ID-TIMS analysis. The six youngest zircon dates are concordant and have indistinguishable isotope ratios with a weighted mean $^{206}Pb/^{238}U$ age of 49.925 ± 0.009 (0.027) [0.060] Ma (MSWD = 1.28; n = 6), which is interpreted to reflect the time since the eruption and deposition of this tuff.

Sixth Tuff

Of 48 zircon crystals analyzed by LA-ICP-MS, nine (19%) returned Cretaceous or older $^{206}Pb/^{238}U$ ages and were excluded from subsequent analyses. Fifteen zircon crystals were selected for CA-ID-TIMS analysis. The seven youngest zircon dates are concordant and have indistinguishable isotope ratios with a weighted mean $^{206}Pb/^{238}U$ of 49.769 ± 0.016 (0.030) [0.061] Ma (MSWD = 1.12; n = 7), which is interpreted to reflect the time since the eruption and deposition of this tuff.

Comparison with Previous Geochronology

Prior work by Smith et al. (2008) and Machlus et al. (2015) identified a potential discrepancy between the U-Pb and $^{40}Ar/^{39}Ar$ ages for the Sixth, Layered, and Main tuffs. While sanidine ages tend to skew younger than zircon U-Pb, due to the difference in closure temperature in these mineral systems, Machlus et al. (2015) found U-Pb ages for these three tuffs that were instead younger than the associated $^{40}Ar/^{39}Ar$ ages from Smith et al. (2008). Machlus proposed this discrepancy may be the result of alteration in the sanidine crystals due to deposition in a hypersaline environment, and that the air abrasion methods used by Smith et al. (2008) may not have sufficiently removed altered rims from the sanidine crystals analyzed.

To resolve this discrepancy, we employed several methods to improve the precision of our U-Pb and $^{40}Ar/^{39}Ar$ ages. Unlike prior work by Smith et al. (2008), we analyzed single crystals, rather than multiple crystal aliquots; this approach eliminates possible contamination by inherited crystals, which can skew the resulting ages older. Additionally, we performed $^{40}Ar/^{39}Ar$ analyses on a Nu Noblesse multi-collector mass spectrometer, allowing us to measure multiple isotopes simultaneously. Furthermore, we used cathodoluminescence imaging when selecting zircons for U-Pb analysis to identify crystals free of inclusions, and we screened zircons based on their LA-ICP-MS age to eliminate inherited cores and crystals from analysis. We also employed a double spike tracer to further improve precision relative to the single-spike tracer used by Machlus et al. (2015).

In the case of the Sixth tuff, our U-Pb age of 49.769 ± 0.016 (0.030) [0.061] Ma is intermediate between the Smith et al. (2008) $^{40}Ar/^{39}Ar$ and Machlus et al. (2015) U-Pb ages, and agrees with both when total uncertainty is considered (Fig. 5). Our U-Pb ages of 49.925 ± 0.009 (0.027) [0.060] Ma for the Layered tuff and 50.114 ± 0.022 (0.034) [0.063] Ma for the Main tuff coincide more closely with the Machlus et al. (2015) U-Pb ages, as does our $^{40}Ar/^{39}Ar$ age of 50.133 ± 0.038 (0.048) [0.078] Ma for the Main tuff, suggesting the younger ages for these tuffs are likely more accurate. Our ages for the remaining tuffs agree with both the Machlus et al. (2015) and Smith et al. (2008) ages within uncertainty (Fig. 5).

In summary, advances in analytical methods and instrumentation have led to improved isotopic data and we consider the results presented here to represent the most accurate age determinations for these tuffs.

Bayesian Age-Depth Modeling

We developed three age-depth models, one each for cores BF-1, CCR-1, and WM (Fig. 6).

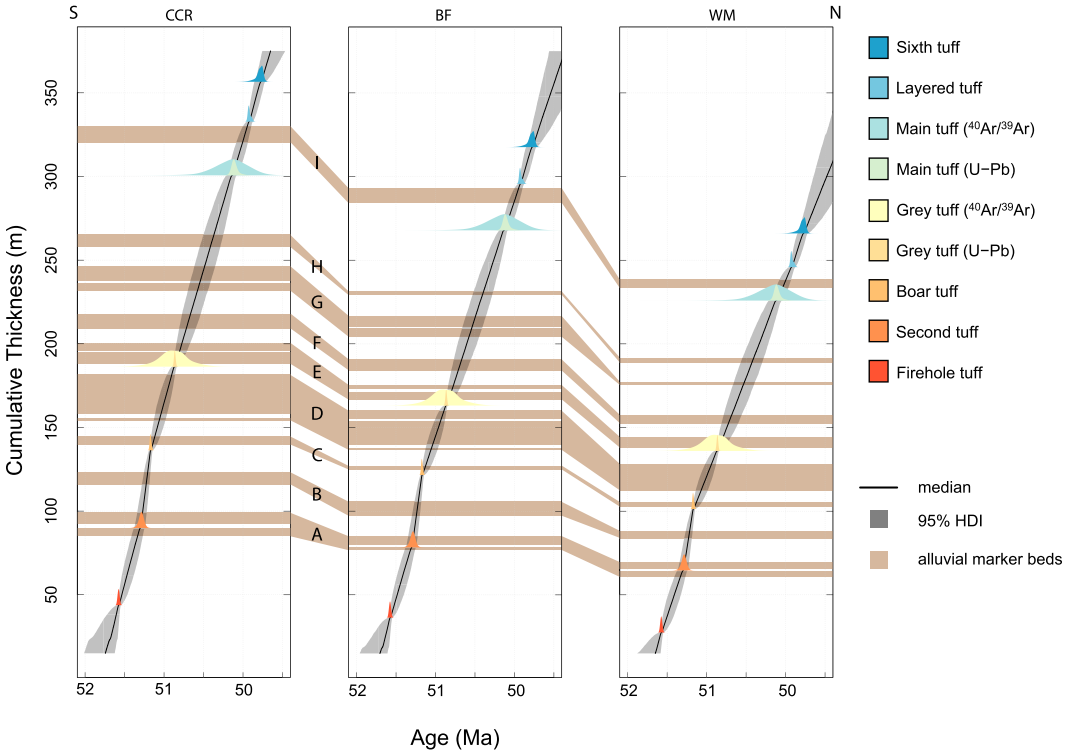

Figure 6. Age models for the Wilkins Peak Member (Green River Formation, Wyoming, USA) in the Blacks Fork (BF)-1, White Mountain (WM), and Currant Creek Ridge (CCR) cores. Shaded distributions represent the summed probability distribution of all U-Pb or $^{40}Ar/^{39}Ar$ analyses for each tuff, as the likelihood inputs. The 95% highest density interval (HDI), indicated by light gray shading, represents the posterior model uncertainty for all interpolated points between tuffs, while the black line indicates the median. All models show a decrease in sedimentation rate at ca. 51 Ma.

Each model is congruent and shows an apparent decrease in accumulation rate between the upper and lower portions of the WPM, with the transition occurring somewhere at or above marker bed C, at ca. 51 Ma (Fig. 6). In core CCR-1, located on the southern margin of the basin, the average accumulation rate decreases from 229 mm/kyr between the Firehole and Boar tuffs, to 158 mm/kyr between the Boar and Sixth tuffs; a 31% decrease in accumulation rate. The overall average accumulation rate for the WPM in core CCR-1 is 173 mm/kyr, and agrees remarkably well with a model of astronomical forcing of sedimentation in this same core which supports an accumulation rate of 169.5 mm/kyr (Meyers, 2008). In core BF-1, which is centrally located in the basin, the average accumulation rates for the same sections are 211 and 141 mm/kyr, respectively, a 33% decrease in accumulation rate. These accumulation rates agree with those inferred by Smith et al. (2010) and Machlus et al. (2015) in the BF-1 core. In core WM, near the northern margin of the basin, the accumulation rate decreases 35%, from 183 to 118 mm/kyr.

Tectonic and Climatic Implications

The observed reduction in accumulation rate after ca. 51 Ma in all three cores coincides with the cessation of faulting along the northern flank of the Uinta uplift (Fig. 7). Uplift along the Uinta fault would have caused flexural subsidence of a southern basin trough (Roehler, 1992), resulting in increased accommodation in the Bridger Basin and relatively rapid accumulation of sediment, including bedded evaporite. As uplift ceased, the reduction in flexural subsidence reduced accommodation space, accumulation rates decreased, and shallowing of the lake prevented the deposition of bedded evaporites (Smith et al., 2008).

To test the association between the alluvial marker beds and eccentricity observed by Smith et al. (2010), we compared the predicted ages for the tops of the marker beds (Table S5) with the ages of peak eccentricity from the orbital solutions of Laskar et al. (2011) and Zeebe and Lourens (2019). The tops of the marker beds were chosen for this comparison because these transitions represent relatively abrupt flooding surfaces (Aswasereelert et al., 2013; Smith et al., 2014) (Fig. 8), suggesting that they are more likely to be isochronous across the basin than the bases of the marker beds, which commonly exhibit evidence of scour (Smith et al., 2015). The upper flooding surfaces of the marker beds are therefore interpreted as optimal targets for comparison with astronomical solutions and the marine record.

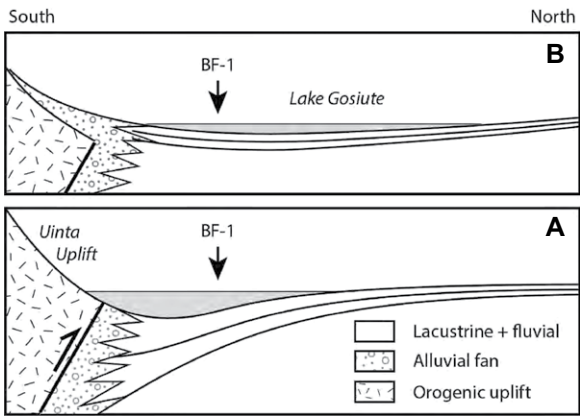

Figure 7. Schematic evolution of the Bridger Basin during deposition of the Wilkins Peak Member of the Green River Formation, Wyoming, USA. BF-1—Blacks Fork #1 core. (A) Prior to marker bed C, Uinta uplift actively thrusting over the southern basin margin resulted in relatively rapid accommodation rates via flexural subsidence of southern basin trough (Roehler, 1992). Sediment accumulation rates were relatively fast, and bedded evaporites were deposited. (B) After marker bed C, cessation of faulting resulted in lower accommodation and sediment accumulation rates, accompanied by an abrupt decrease in bedded evaporite deposition (Wiig et al., 1995; Smith et al., 2008).

Figure 8. Outcrop photo of the D marker bed of the Wilkins Peak Member of the Green River Formation, Wyoming, USA. The abrupt, flat surface at the top of the section is interpreted as a flood surface that exhibits little evidence of scour and is therefore more likely to reflect isochronous deposition across the basin.

Of the nine marker beds, the upper six display a close association between the median predicted age of the top of the marker bed and eccentricity maxima in both the Laskar et al. (2011) and Zeebe and Lourens (2019) astronomical solutions (Fig. 9). Of note, all six marker bed flooding surfaces that coincide with eccentricity maxima occur in succession and were deposited after the observed shift in sedimentation rate at ca. 51 Ma. To quantify this association, we employed the Rayleigh test for phase directionality, using the *rayleigh.test* function of the R package "circular" (Agostinelli and Lund, 2017) and the *hilbert* and *resample* functions of the R package "astrochron" (Meyers, 2014). We adopt as a formal null hypothesis (H_0) that alluvial-lacustrine transitions are independent of eccentricity maxima, and the alternative hypothesis (H_1) that alluvial-lacustrine transitions are paced by eccentricity maxima. The phase of eccentricity associated with these paleoenvironmental transitions is determined using the Bayesian age-depth model of core BF-1 to determine the median age for the top of each marker bed, which is then used to sample the phase of eccentricity in the astronomical solution, determined via Hilbert transform. The results for the La10b eccentricity solution (Laskar et al., 2011) are shown in Figure 10, since it was used to tune the benthic *N. truempyi* $\delta^{13}C$ and $\delta^{18}O$ records of Ocean Drilling Program Site 1263 of Lauretano et al. (2018), and therefore permits direct comparison with the marine record. Other astronomical solutions are also evaluated (Fig. 11).

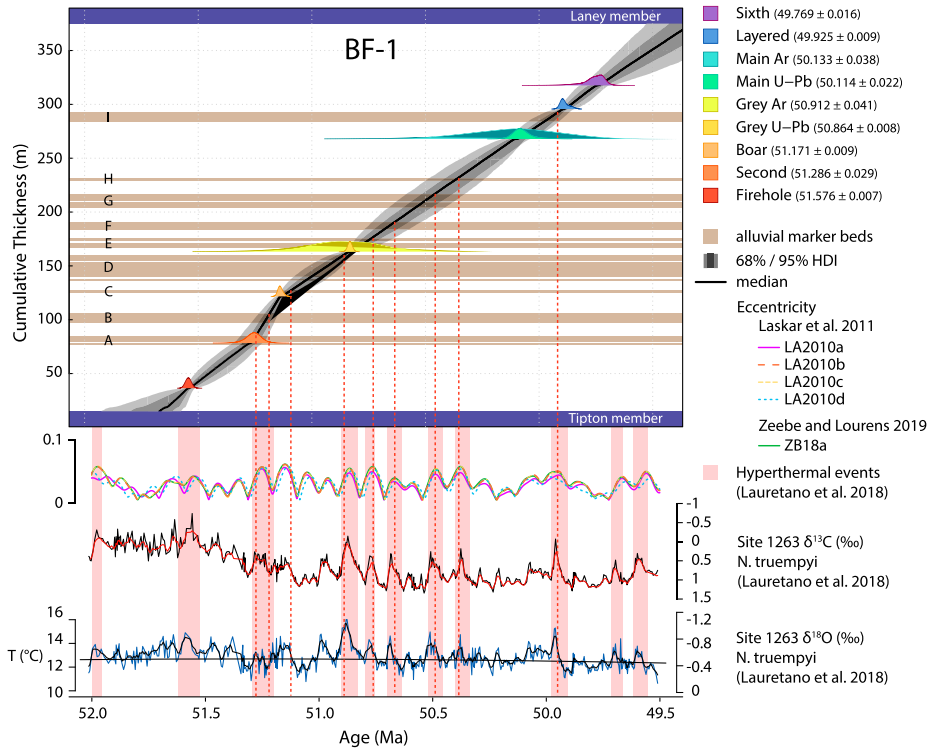

Figure 9. Age model for the Blacks Fork (BF)-1 core and projection of age-calibrated sedimentological variability in the Wilkins Peak Member of the Green River Formation (Wyoming, USA) onto astronomical solutions and global climate proxy records. Vertical dashed red lines indicate the modeled age associated with the top of each marker bed, which are compared with the eccentricity solutions of Laskar et al. (2011) and Zeebe and Lourens (2019), and with the benthic *N. truempyi* $\delta^{13}C$ and $\delta^{18}O$ records from Ocean Drilling Program Site 1263 of Lauretano et al. (2018). HDI—highest density interval; T—temperature.

The observed eccentricity phase angles produce a Rayleigh test value $R = 0.6835$, with a p-value of 0.0012, thus we reject H_0 (Fig. 10). This strong correlation between an untuned sedimentary record and a key theoretical eccentricity solution convincingly supports the findings of Smith et al. (2010, 2014), Aswasereelert et al. (2013), and Machlus et al. (2015) that alluvial marker bed deposition was paced by short eccentricity. When this test is applied only to the upper six consecutive marker beds, the Rayleigh test value improves to $R = 0.8098$ (p-value of 0.0013), suggesting that cessation of uplift along the Uinta fault and the accompanying reduction of accommodation space rendered the basin more susceptible to astronomical forcing, or more capable of preserving such signals (Fig. 10).

Our model also indicates a relationship specifically between marker bed deposition and rising eccentricity. Eccentricity primarily influences Earth's climate system through amplitude modulation of precession, potentially driving variations in seasonality, precipitation, and physical and chemical weathering across different phases of eccentricity (e.g., Zachos et al., 2010; Birgenheier et al., 2020). Recent findings in early Eocene marine strata suggest that the carbon isotope excursion associated with the Paleocene-Eocene thermal maximum and earlier carbon cycle perturbations were triggered by climate changes and light carbon release to the oceans that reflect the rise to maxima in short eccentricity (Piedrahita et al., 2022).

In the Bridger Basin, our model suggests that increasing eccentricity enhanced delivery of lowstand alluvial sediment onto the desiccated lake floor, possibly due to increased seasonality, "monsoon-like" precipitation, and increased physical and chemical weathering (e.g., Zachos et al., 2010; Birgenheier et al., 2020). Alluvial sediments dominated deposition in the basin under rising eccentricity until reaching peak

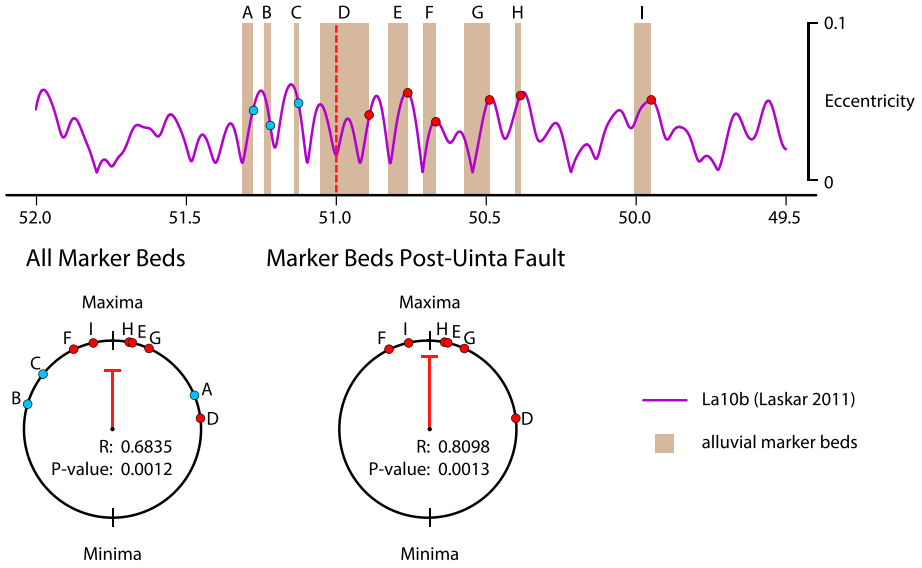

Figure 10. The Rayleigh test for phase directionality. Eccentricity phase is sampled at the modeled age of the top of each marker bed in the Wilkins Peak Member of the Green River Formation, Wyoming, USA. Prior to ca. 51 Ma (indicated by dashed red line), the Uinta uplift was actively thrusting over the southern basin margin, resulting in relatively rapid accommodation rates and sediment accumulation (Roehler, 1992). Phase angles sampled from this time are shown as blue dots. After ca. 51 Ma, cessation of faulting lowered accommodation and sediment accumulation rates (Smith et al., 2008). Phase angles sampled from this time span are shown as red dots. The sampled phase angle from all nine marker beds produces R = 0.6835, with a p-value of 0.0012, allowing us to reject H_0. R is "Rayleigh's R," which is a measure of the spread of multiple vectors about their average direction. We use it to evaluate the phase directionality between marker bed flooding surfaces and eccentricity maxima. The p-value is the probability of rejecting the null hypothesis (Ho) in error. The null hypothesis being tested (Ho) is that alluvial-lacustrine transitions are independent of eccentricity maxima, and the alternative hypothesis (H1) is that alluvial-lacustrine transitions are paced by eccentricity maxima. When only the upper six beds are considered, R increases to 0.8098 (p-value = 0.0013).

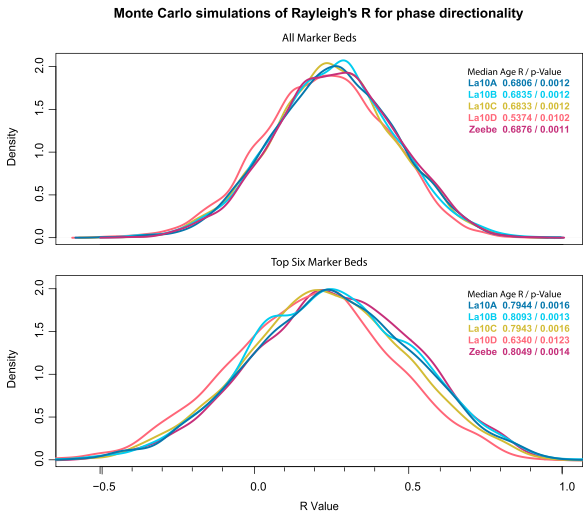

Figure 11. Monte Carlo simulations of Rayleigh's R for phase directionality. The R and p-values listed in the upper right are those associated with the median predicted age of the tops of alluvial marker beds A-I in core Blacks Fork (BF)-1 from the Wilkins Peak Member of the Green River Formation (Wyoming, USA) using five different orbital solutions. Colored curves represent the R values of 5000 iterations of the Rayleigh test using predicted ages for the top of each marker bed pulled from the 95% highest density interval of the Bayesian model for core BF-1. Predicted ages were drawn from the Monte Carlo generated age-depth paths produced in the Bayesian modeling process, and so honor the principle of superposition. The top plot shows results for all nine marker bed tops. The probability distribution of Monte Carlo simulated R is clustered around ~0.3 for most astronomical solutions, in contrast to the ~0.7 values produced by using the median modeled age (the most likely model). The lower plot shows results for the upper six consecutive marker beds.

eccentricity, during which further intensification of seasonality appears to have shifted the hydrologic budget of the Bridger Basin, altering accommodation by moving the locus of alluvial sedimentation toward the basin margins and drowning alluvial deposits nearer to the basin center. This interpretation contrasts with Smith et al. (2014), who argue that lacustrine deposits of the WPM, including bedded evaporites that record expansion and contraction of the lake, reflect greater seasonality and precipitation fluctuations expected during periods of high eccentricity. Accordingly, Smith et al. (2014) propose that climatically drier and more stable periods associated with eccentricity minima led to deposition of the alluvial marker beds.

Our findings and interpretations differ in detail from those of Smith et al. (2014) in large part because new U-Pb zircon ages are significantly more precise than previous geochronology in Machlus et al. (2015) and Smith et al. (2008, 2010), and the ages are integrated using Bayesian age-depth modeling. However, despite these advances, further work is needed to refine the pacing of alluvial marker bed deposition during maxima in orbital eccentricity. This need for further refinement is apparent in the observation that, whereas the median predicted ages of the alluvial marker bed tops in our Bayesian model—the statistically most likely ages—show a strong association with eccentricity maxima, Monte Carlo simulations using the full 95% HDI envelope of the Bayesian model produce R values closer to ~0.3 with reduced statistical significance (Fig. 11). From this degraded significance, we conclude that the conservative error envelope resulting from the extrapolation between dated tuffs in our Bayesian age-depth modeling algorithm is likely over-estimated. U-Pb ages from tuffs that have yet to be dated, coupled with additional, more precise, $^{40}Ar/^{39}Ar$ dates from several tuffs, are needed to reduce the uncertainty envelope of the Bayesian model, and thus better constrain the tempo and genesis of the alluvial marker beds and their relationship with the phase of eccentricity.

CONCLUSIONS

$^{206}Pb/^{238}U$ zircon and $^{40}Ar/^{39}Ar$ sanidine ages from tuffs in the WPM are concordant and sufficiently precise to resolve discrepancies between the two chronometers noted in previous work. The Bayesian approach integrates these clocks into a single age-depth model, with a two- to tenfold increase in temporal resolution compared to previous radioisotopic age models for the WPM. This model reveals basin-scale changes in sedimentation rate coincident with cessation of faulting along the Uinta uplift at ca. 51 Ma,

suggesting a uniform and rapid reduction in flexural subsidence as a likely driver for reduced sediment accumulation. Our new age model also permits a direct comparison between an untuned terrestrial sedimentary record and theoretical astronomical solutions, which suggests a close association between the deposition of nine alluvial marker beds and the phasing of orbital eccentricity. In our proposed model, flooding surfaces atop six of these alluvial beds correspond with short eccentricity maxima. Confirming this terrestrial response of climate and the hydrologic cycle to increasing eccentricity, during the Eocene greenhouse, is within reach of Bayesian age-depth models that integrate additional radioisotopic ages of tuffs. Our findings thus motivate further efforts to correlate between terrestrial and marine records of responses to astronomically driven climate change.

ACKNOWLEDGMENTS

This contribution represents Bruck's MSc thesis at the University of Wisconsin–Madison. We thank James Crowley, Debbie Pierce, and Bryan Wathen for assistance in the labs, Robin Trayler for guidance regarding the modified Bchron package, and Mike Smith for his comments on, and discussion of, the manuscript. Comments of two anonymous reviewers propelled us to clarify many points and are greatly appreciated. This research was supported by National Science Foundation–Division of Earth Sciences grants 1813278 (Carroll, Singer, Meyers) and 1813088 (Schmitz), an ExxonMobil/Geological Society of America graduate research grant (Walters), an American Association of Petroleum Geologists Foundation grant-in-aid (Walters), and the Department of Geoscience at the University of Wisconsin–Madison.

REFERENCES CITED

Agostinelli, C., and Lund, U., 2017, R package 'circular': Circular Statistics (version 0.4-93), https://r-forge.r-project.org/projects/circular/.

Aswasereelert, W., Meyers, S.R., Carroll, A.R., Peters, S.E., Smith, M.E., and Feigl, K.L., 2013, Basin-scale cyclostratigraphy of the Green River Formation, Wyoming: Geological Society of America Bulletin, v. 125, p. 216–228, https://doi.org/10.1130/B30541.1.

Birgenheier, L.P., Berg, M.D.V., Plink-Björklund, P., Gall, R.D., Rosencrans, E., Rosenberg, M.J., Toms, L.C., and Morris, J., 2020, Climate impact on fluvial-lake system evolution, Eocene Green River Formation, Uinta Basin, Utah, USA: Geological Society of America Bulletin, v. 132, p. 562–587, https://doi.org/10.1130/B31808.1.

Bradley, W.H., 1929, The varves and climate of the Green River epoch: U.S. Geological Survey Professional Paper, v. 158, p. 87–110, https://doi.org/10.3133/pp158E.

Brownfield, M.E., Self, J.G., and Mercier, T.J., 2011, Fischer assay histograms of oil-shale drill cores and rotary cuttings from the Great Divide, Green River, and Washakie basins, southwestern Wyoming, *in* Oil Shale Resources of the Eocene Green River Formation, Greater Green River Basin, Wyoming, Colorado, and Utah: U.S. Geological Survey Digital Data Series, p. 1–9.

Condon, D., Schoene, B., McLean, N., Bowring, S., and Parrish, R., 2015, Metrology and traceability of U-Pb isotope dilution geochronology (EARTHTIME Tracer Calibration Part I): Geochimica et Cosmochimica Acta, v. 164, p. 464–480, https://doi.org/10.1016/j.gca.2015.05.026.

Culbertson, W.C., 1961, Stratigraphy of the Wilkins Peak Member of the Green River Formation, Firehole Basin quadrangle, Wyoming, *in* Short Articles in the Geologic and Hydrologic Sciences, articles 293–495: U.S. Geological Survey Professional Paper, v. 424-D, p. 170–173.

Cramer, B.S., Wright, J.D., Kent, D.V., and Aubry, M.P., 2003, Orbital climate forcing of $\delta^{13}C$ excursions in the late Paleocene-early Eocene (chrons C24n-C25n): Paleoceanography and Paleoclimatology, v. 18, p. 1–25, https://doi.org/10.1029/2003PA000909.

Fischer, A.G., and Roberts, L.T., 1991, Cyclicity in the Green River Formation (lacustrine Eocene) of Wyoming: Journal of Sedimentary Petrology, v. 61, p. 1146–1154.

Haslett, J., and Parnell, A.C., 2008, A simple monotone process with application to radiocarbon-dated depth chronologies: Applied Statistics, v. 57, no. 4, p. 399–418.

Jagniecki, E.A., Lowenstein, T.K.T.K., Jenkins, D.M., and Demicco, R.V., 2015, Eocene atmospheric CO_2 from the nahcolite proxy: Geology, v. 43, p. 1075–1078, https://doi.org/10.1130/G36886.1.

Jicha, B.R., Singer, B.S., and Sobol, P., 2016, Re-evaluation of the ages of $^{40}Ar/^{39}Ar$ sanidine standards and supereruptions in the western U.S. using a Noblesse multi-collector mass spectrometer: Chemical Geology, v. 431, p. 54–66, https://doi.org/10.1016/j.chemgeo.2016.03.024.

Kuiper, K.F., Deino, A., Hilgen, F.J., Krijgsman, W., Renne, P.R., and Wijbrans, J.R., 2008, Synchronizing rock clocks of earth history: Science, v. 320, p. 500–504, https://doi.org/10.1126/science.1154339.

Laskar, J., Robutel, P., Joutel, F., Gastineau, M., Correia, A.C.M., and Levrard, B., 2004, A long-term numerical solution for the insolation quantities of the Earth: Astronomy & Astrophysics, v. 428, p. 261–285, https://doi.org/10.1051/0004-6361:20041335.

Laskar, J., Fienga, A., Gastineau, M., and Manche, H., 2011, La2010: A new orbital solution for the long-term motion of the Earth: Astronomy & Astrophysics, v. 532, p. 1–15, https://doi.org/10.1051/0004-6361/201116836.

Lauretano, V., Hilgen, F.J., Zachos, J.C., and Lourens, L.J., 2016, Astronomically tuned age model for the early Eocene carbon isotope events: A new high-resolution $\delta^{13}C$ benthic record of ODP Site 1263 between ~49 and ~54 Ma: Newsletters on Stratigraphy, v. 49, p. 383–400, https://doi.org/10.1127/nos/2016/0077.

Lauretano, V., Zachos, J.C., and Lourens, L.J., 2018, Orbitally paced carbon and deep-sea temperature changes at the peak of the early Eocene climatic optimum: Paleoceanography and Paleoclimatology, v. 33, no. 10, p. 1050–1065, https://doi.org/10.1029/2018PA003422.

Machlus, M., Hemming, S.R., Olsen, P.E., and Christie-Blick, N., 2004, Eocene calibration of geomagnetic polarity time scale reevaluated: Evidence from the Green River Formation in Wyoming: Geology, v. 32, p. 137–140, https://doi.org/10.1130/G20091.1.

Machlus, M.L., Olsen, P.E., Christie-Blick, N., and Hemming, S.R., 2008, Spectral analysis of the lower Eocene Wilkins Peak Member, Green River Formation, Wyoming: Support for Milankovitch cyclicity: Earth and Planetary Science Letters, v. 268, p. 64–75, https://doi.org/10.1016/j.epsl.2007.12.024.

Machlus, M.L., Ramezani, J., Bowring, S.A., Hemming, S.R., Tsukui, K., and Clyde, W.C., 2015, A strategy for cross-calibrating U-Pb chronology and astrochronology of sedimentary sequences: An example from the Green River Formation, Wyoming, USA: Earth and Planetary Science Letters, v. 413, p. 70–78, https://doi.org/10.1016/j.epsl.2014.12.009.

Mattinson, J.M., 2005, Zircon U-Pb chemical abrasion ("CA-TIMS") method: Combined annealing and multi-step partial dissolution analysis for improved precision and accuracy of zircon ages: Chemical Geology, v. 220, p. 47–66, https://doi.org/10.1016/j.chemgeo.2005.03.011.

McInerney, F.A., and Wing, S.L., 2011, The Paleocene-Eocene thermal maximum: A perturbation of carbon cycle, climate, and biosphere with implications for the future: Annual Review of Earth and Planetary Sciences, v. 39, p. 489–516, https://doi.org/10.1146/annurev-earth-040610-133431.

McLean, N.M., Condon, D.J., Schoene, B., and Bowring, S.A., 2015, Evaluating uncertainties in the calibration of isotopic reference materials and multi-element isotopic tracers (EARTHTIME Tracer Calibration Part II): Geochimica et Cosmochimica Acta, v. 164, p. 481–501, https://doi.org/10.1016/j.gca.2015.02.040.

Meyers, S.R., 2008, Resolving Milankovitchian controversies: The Triassic Latemar limestone and the Eocene Green River Formation: Geology, v. 36, p. 319–322, https://doi.org/10.1130/G24423A.1.

Meyers, S.R., 2014, Astrochron: An R Package for Astrochronology, https://cran.r-project.org/package=astrochron (accessed 6 October 2021).

Min, K., Mundil, R., Renne, P.R., and Ludwig, K.R., 2000, A test for systematic errors in $^{40}Ar/^{39}Ar$ geochronology through comparison with U/Pb analysis of a 1.1-Ga rhyolite: Geochimica et Cosmochimica Acta, v. 64, p. 73–98, https://doi.org/10.1016/S0016-7037(99)00204-5.

Piedrahita, V.A., Galeotti, S., Zhao, X., Roberts, A.P., Rohling, E.J., Heslop, D., Florindo, F., Grant, K.M., Rodríguez-Sanz, L., Reghellin, D., and Zeebe, R.E., 2022, Orbital phasing of the Paleocene-Eocene Thermal Maximum: Earth and Planetary Science Letters, v. 598, https://doi.org/10.1016/j.epsl.2022.117839.

Pietras, J.T., and Carroll, A.R., 2006, High-resolution stratigraphy of an underfilled lake basin: Wilkins Peak member, Eocene Green River Formation, Wyoming, USA: Journal of Sedimentary Research, v. 76, no. 11, p. 1197–1214, https://doi.org/10.2110/jsr.2006.096.

Renne, P.R., Balco, G., Ludwig, K.R., Mundil, R., and Min, K., 2011, Response to the comment by W.H. Schwarz et al. on "Joint determination of ^{40}K decay constants and $^{40}Ar^*/^{40}K$ for the Fish Canyon sanidine standard, and improved accuracy for $^{40}Ar/^{39}Ar$ geochronology" by P.R. Renne et al. (2010): Geochimica et Cosmochimica Acta, v. 75, no. 17, p. 5097–5100, https://doi.org/10.1016/j.gca.2011.06.021.

Rivera, T.A., Schmitz, M.D., Crowley, J.L., and Storey, M., 2014, Rapid magma evolution constrained by zircon petrochronology and $^{40}Ar/^{39}Ar$ sanidine ages for the Huckleberry Ridge Tuff, Yellowstone, USA: Geology, v. 42, p. 643–646, https://doi.org/10.1130/G35808.1.

Roehler, H.W., 1992, Correlation, composition, areal distribution, and thickness of Eocene stratigraphic units, greater Green River basin, Wyoming, Utah, and Colorado: U.S. Geological Survey Professional Paper, v. 1506-E, https://doi.org/10.3133/pp1506E.

Smith, M.E., Carroll, A.R., and Singer, B.S., 2008, Synoptic reconstruction of a major ancient lake system: Eocene Green River Formation, western United States: Geological Society of America Bulletin, v. 120, p. 54–84, https://doi.org/10.1130/B26073.1.

Smith, M.E., Chamberlain, K.R., Singer, B.S., and Carroll, A.R., 2010, Eocene clocks agree: Coeval $^{40}Ar/^{39}Ar$, U-Pb, and astronomical ages from the Green River Formation: Geology, v. 38, p. 527–530, https://doi.org/10.1130/G30630.1.

Smith, M.E., Carroll, A.R., Scott, J.J., and Singer, B.S., 2014, Early Eocene carbon isotope excursions and landscape destabilization at eccentricity minima: Green River Formation of Wyoming: Earth and Planetary Science Letters, v. 403, p. 393–406, https://doi.org/10.1016/j.epsl.2014.06.024.

Smith, M.E., Carroll, A.R., and Scott, J.J., 2015, Stratigraphic expression of climate, tectonism, and geomorphic forcing in an underfilled lake basin: Wilkins Peak Member of the Green River Formation, *in* Smith, M.E., and Carroll, A.R., eds., Stratigraphy and Paleolimnology of the Green River Formation, Western USA: Dordrecht, Netherlands, Springer, p. 61–102, https://doi.org/10.1007/978-94-017-9906-5_4.

Trayler, R.B., Schmitz, M.D., Cuitiño, J.I., Kohn, M.J., Bargo, M.S., Kay, R.F., Strömberg, C.A.E., and Vizcaíno, S.F., 2020, An improved approach to age-modeling in deep time: Implications for the Santa Cruz Formation, Argentina: Geological Society of America Bulletin, v. 132, p. 233–244, https://doi.org/10.1130/B35203.1.

Westerhold, T., Röhl, U., Frederichs, T., Agnini, C., Raffi, I., Zachos, J.C., and Wilkens, R.H., 2017, Astronomical calibration of the Ypresian timescale: Implications for seafloor spreading rates and the chaotic behavior of the solar system?: Climate of the Past, v. 13, no. 9, p. 1129–1152, https://doi.org/10.5194/cp-13-1129-2017.

Wiig, S.V., Gundy, W.D., and Dyni, J.R., 1995, Trona resources in the Green River basin, southwest Wyoming: U.S. Geological Survey Open-File Report, v. OF 95-476, 91 p.

Wotzlaw, J.F., Schaltegger, U., Frick, D.A., Dungan, M.A., Gerdes, A., and Günther, D., 2013, Tracking the evolution of large-volume silicic magma reservoirs from assembly to supereruption: Geology, v. 41, p. 867–870, https://doi.org/10.1130/G34366.1.

Zachos, J.C., Dickens, G.R., and Zeebe, R.E., 2008, An early Cenozoic perspective on greenhouse warming and carbon-cycle dynamics: Nature, v. 451, p. 279–283, https://doi.org/10.1038/nature06588.

Zachos, J.C., McCarren, H., Murphy, B., Röhl, U., and Westerhold, T., 2010, Tempo and scale of late Paleocene and early Eocene carbon isotope cycles: Implications for the origin of hyperthermals: Earth and Planetary Science Letters, v. 299, p. 242–249, https://doi.org/10.1016/j.epsl.2010.09.004.

Zeebe, R.E., and Lourens, L.J., 2019, Solar system chaos and the Paleocene-Eocene boundary age constrained by geology and astronomy: Science, v. 365, p. 1–18.

Zeebe, R.E., Zachos, J.C., and Dickens, G.R., 2009, Carbon dioxide forcing alone insufficient to explain Palaeocene–Eocene Thermal Maximum warming: Nature Geoscience, v. 2, p. 576–580, https://doi.org/10.1038/ngeo578.

Zhu, J., Poulsen, C.J., and Tierney, J.E., 2019, Simulation of Eocene extreme warmth and high climate sensitivity through cloud feedbacks: Science Advances, v. 5, https://doi.org/10.1126/sciadv.aax1874.

Science Editor: Wenjiao Xiao
Associate Editor: Daniel Peppe

Manuscript Received 13 May 2022
Revised Manuscript Received 11 November 2022
Manuscript Accepted 26 January 2023

Printed in the USA